



# A Ship-Based Characterization of Coherent Boundary-Layer Structures Over the Lifecycle of a Marine Cold-Air Outbreak

Christiane Duscha<sup>1</sup> · Christopher Barrell<sup>2</sup> · Ian A. Renfrew<sup>2</sup> ·  
Ian M. Brooks<sup>3</sup> · Harald Sodemann<sup>4</sup> · Joachim Reuder<sup>1</sup>

Received: 8 February 2021 / Accepted: 22 January 2022  
© The Author(s) 2022

## Abstract

Convective coherent structures shape the atmospheric boundary layer over the lifecycle of marine cold-air outbreaks (CAOs). Aircraft measurements have been used to characterize such structures in past CAOs. Yet, aircraft case studies are limited to snapshots of a few hours and do not capture how coherent structures, and the associated boundary-layer characteristics, change over the CAO time scale, which can be on the order of several days. We present a novel ship-based approach to determine the evolution of the coherent-structure characteristics, based on profiling lidar observations. Over the lifecycle of a multi-day CAO we show how these structures interact with boundary-layer characteristics, simultaneously obtained by a multi-sensor set-up. Observations are taken during the Iceland Greenland Seas Project's wintertime cruise in February and March 2018. For the evaluated CAO event, we successfully identify cellular coherent structures of varying size in the order of  $4 \times 10^2$  m to  $10^4$  m and velocity amplitudes of up to  $0.5 \text{ m s}^{-1}$  in the vertical and  $1 \text{ m s}^{-1}$  in the horizontal. The structures' characteristics are sensitive to the near-surface stability and the Richardson number. We observe the largest coherent structures most frequently for conditions when turbulence generation is weakly buoyancy dominated. Structures of increasing size contribute efficiently to the overturning of the boundary layer and are linked to the growth of the convective boundary-layer depth. The new approach provides robust statistics for organized convection, which would be easy to extend by additional observations during convective events from vessels of opportunity operating in relevant areas.

**Keywords** Cold-air outbreak · Convective coherent structures · Iceland–Greenland sea · Lidar wind profiling

---

✉ Christiane Duscha  
christiane.duscha@uib.no

<sup>1</sup> Geophysical Institute, Bergen Offshore Wind Center and Bjerknes Centre for Climate Research, University of Bergen, Post box 7803, 5020 Bergen, Norway

<sup>2</sup> School of Environmental Sciences, University of East Anglia, Norwich, UK

<sup>3</sup> School of Earth and Environment, University of Leeds, Leeds, UK

<sup>4</sup> Geophysical Institute and Bjerknes Centre for Climate Research, University of Bergen, Bergen, Norway

# 1 Introduction

Large temperature differences between the atmosphere and ocean typically develop due to the advection of cold air over a warmer ocean surface. This process is often referred to as a marine cold-air outbreak (CAO). The elevated turbulent fluxes of sensible and latent heat initiated by the large air–sea temperature contrast can easily reach several hundreds of  $\text{W m}^{-2}$ , or, in extreme cases, even exceed  $1000 \text{ W m}^{-2}$  (Grossman and Betts 1990). Organized convective structures contribute an essential part to these compensating fluxes. Detailed statistical sampling of the parameters necessary to characterize these structures is still sparse in the relevant regions. During the Iceland–Greenland Seas Project (IGP) in February and March 2018 we observed several CAO events from aboard the *NRV Alliance* (Renfrew et al. 2019). For one of these CAOs we investigate the impact of organized convective-structure development on the evolution of the instabilities and the turbulent fluxes.

The heat fluxes during CAOs typically result in significant boundary-layer warming and moistening (e.g., Papritz and Spengler 2017). Further, Papritz and Sodemann (2018) found that CAOs create an intense local water cycle, with rapid turnover of water vapour associated with a distinct signature in the stable water isotope composition (Thurnherr et al. 2020). The warming and moistening of the atmosphere occurs at the expense of ocean surface-layer cooling and salinification, important drivers for the formation of dense water and thus important for the global ocean circulation (Buckley and Marshall 2016). The turbulent heat fluxes into the atmospheric boundary layer also play an important role for the maturing of polar lows responsible for high-impact weather conditions in the Nordic Seas and the adjacent coasts (e.g., Førre et al. 2011). Consequently, regional weather as well as the global climate system are directly affected by elevated turbulent heat fluxes during CAOs.

Organized convection, which results in coherent structures in the wind, temperature, and moisture fields, was found to contribute an essential part to these turbulent heat fluxes (e.g., LeMone 1973; Chou and Ferguson 1991; Brilouet et al. 2020). Mesoscale shallow convection patterns, such as roll vortices, open cellular convection, and closed cellular convection, are generally affiliated with marine CAO events (Atkinson and Zhang 1996). Even though these mesoscale structures have received major attention in the past, small-scale cellular structures, comparable to cellular Rayleigh–Bénard convection, studied in laboratory experiments, are also important in the convective marine atmospheric boundary layer (MABL) (Cieszelski 1998). Mesoscale convection often manifests in the form of organized cloud patterns clearly seen in satellite images. However, characterizing small-scale convection requires more detailed observations of the meteorological variables, such as wind speed and direction, in the MABL.

Previous case studies of marine CAOs have identified coherent-structure characteristics from research aircraft measurements (Atlas et al. 1986; Chang and Braham 1991; Brümmer 1996; Hartmann et al. 1997; Cieszelski 1998; Renfrew and Moore 1999; Cook and Renfrew 2015; Brilouet et al. 2017). These studies determined coherent-structure characteristics, such as along and across wind asymmetries, the wavelength and aspect ratio of roll vortices, and snapshots of the turbulence characteristics throughout the MABL. Yet research flights only have a few hours to sample. Thus, the estimated characteristics of coherent structures are averages over short periods, and the evolution of coherent structures in time remains poorly sampled. Hence, achieving detailed statistical sampling of coherent structures during CAO conditions is an important goal of this study.

Here, we utilize ship-based observations from the Iceland and Greenland Seas region, obtained by a multi-sensor set-up during the IGP campaign. A distinct CAO case forms

the basis of our study. We sampled profiles of the core MABL variables, such as temperature, humidity, precipitation, and wind with three remote-sensing instruments: a passive microwave radiometer, a micro rain radar, and a wind-profiling Doppler lidar. The resulting observations provide improved temporal and vertical resolutions compared to those provided by aircraft measurements. Brooks et al. (2017) demonstrate the large potential of such multi-sensor and ship-based MABL estimates, utilizing a similar set of remote-sensing instrumentation. Nonetheless, the sampling of coherent structures remains challenging with the available instrumentation and from aboard a ship exposed to wave motion. Here, we use motion-compensated lidar observations to identify coherent structures and investigate their temporal development. Such an improved statistical sampling of the coherent structures over the lifecycle of CAOs directly contributes to the overall goal of the IGP mission. The project aims to identify and characterize the exact atmospheric mechanisms, including the impact of coherent structures, involved in the high-latitude water mass transformations. In this study, we provide the methodology to estimate the coherent-structure characteristics from observations over the lifecycle of a CAO, evaluate the inter-dependency of the structures' characteristics, and evaluate the processes which link the structure evolution to the respective boundary-layer characteristics.

## 2 The Iceland and Greenland Seas' Cruise

We focus on the ship-based part of the IGP campaign, which lasted 43 days, starting on 6 February and terminating on 21 March 2018 in Reykjavik, Iceland. For an overview of the entire IGP campaign as well as the major atmospheric and oceanic events over the corresponding observational period we refer the reader to Renfrew et al. (2019). The cruise on the *NRV Alliance* covered an area of the Iceland and southern Greenland Seas. Over the course of the cruise, Renfrew et al. (2019) identified several marine CAOs, of which we study one in more detail. Figure 1 shows a map of the study area relevant to the IGP cruise (Fig. 1a) and a close up of the area relevant to the ship track corresponding to the evaluated CAO event from 28 February to 3 March (Fig. 1b). Also displayed are radiosonde launches along the track, as well as the sea-surface temperature, *SST*, and the sea-ice cover averaged over the evaluated CAO period.

### 2.1 Ship-Based Observations

Time series of air temperature,  $T_a$ ; relative humidity,  $RH$ ; pressure,  $P$ ; wind speed,  $ws$ ; and wind direction,  $wd$ , were sampled with a 1-min time resolution by three automatic weather stations, situated on the bow mast of the *NRV Alliance* at  $\approx 15$  m above sea level. Also, the sea-surface temperature was measured continuously at the bow of the ship using a digital oceanographic thermometer (SBE 38, Sea-Bird Scientific, Bellevue, USA). The data are fully quality controlled (see Renfrew et al. 2021) and time series of measurements are combined and made available by Barrell and Renfrew (2020) in the Centre for Environmental Data Analysis (CEDA) archive.

In addition to the instruments permanently installed on the ship we installed several sensors to obtain a wider range of variables and, in particular, atmospheric profiles of  $T_a$ ,  $RH$ , the three-dimensional wind vector,  $\mathbf{u}$ , and precipitation properties, in particular the terminal or fall velocity of precipitating particles,  $v_f$ . These instruments included a Doppler wind-profiling lidar (WindCube V2 Offshore 8.66, Leosphere, Orsay, France), a micro rain radar

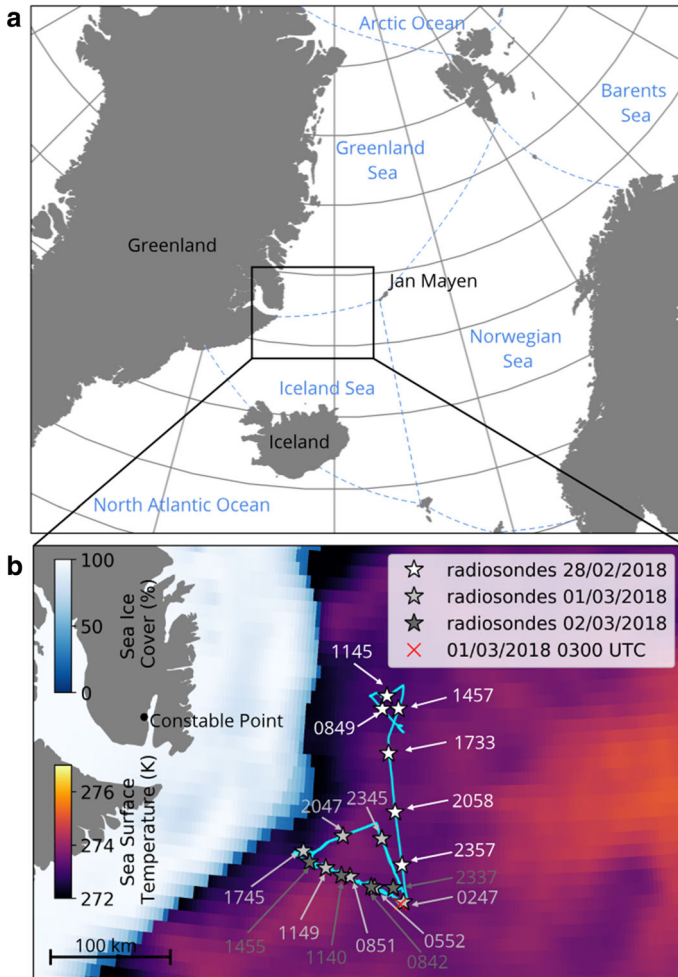


**Fig. 1** **a** Overview of the area relevant to the IGP cruise and **b** close-up of the study area in the Greenland and Iceland Seas relevant to the CAO event from 28 February to 3 March, the corresponding track of the *NRV Alliance* as well as the corresponding average SST, and sea-ice cover from the GHRSSST satellite product. Locations and time (UTC) of the ship corresponding to radiosonde launches are indicated along the track. The red cross marks the location of the ship during the example situation discussed in Sect. 4. (Color figure online)

(MRR-2, Metek, Elmshorn, Germany), a cavity ring-down spectrometer (L2140-i Ser. No. HIDS2254, Picarro Inc, Sunnyvale, USA) for stable water isotope analysis, and a passive microwave radiometer (RPG-HATPRO-G4, Radiometer Physics GmbH, Meckenheim, Germany). The radiometer was situated on a single axis motion-correction table, following Achtert et al. (2015), to compensate for the roll motion of the ship and minimize motion errors during boundary-layer scans. Ship motion was removed during post-processing from the lidar observations, as described by Duscha et al. (2020). Radar retrievals were re-processed to improve the data for snow-dominated precipitation (Maahn and Kollias 2012). Figure 2 shows the location of the instrumentation during the IGP cruise. The lidar, the radiometer,

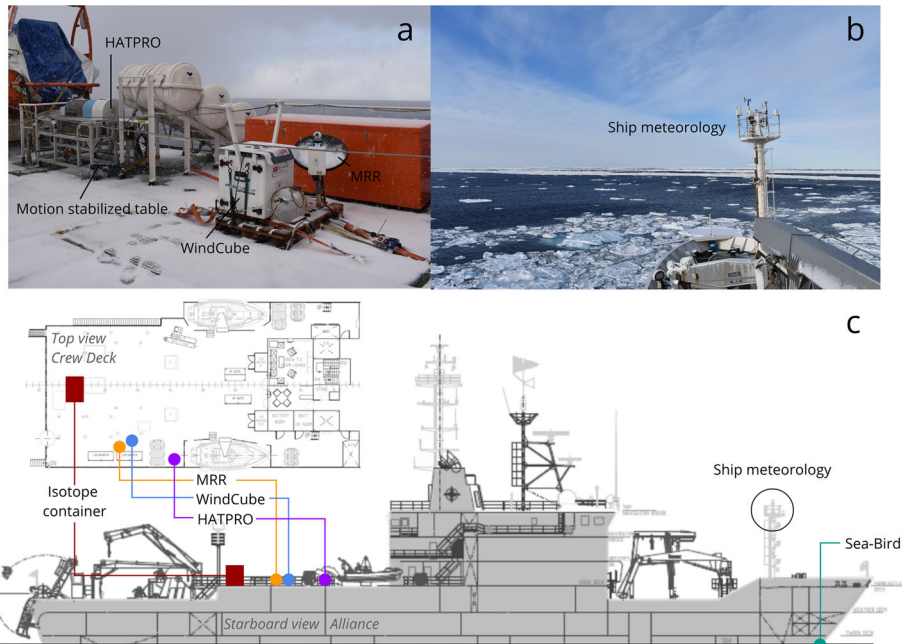


**Fig. 2** Set-up of instrumentation utilized during the IGP campaign on the *NRV Alliance*. **a** Photos of the remote sensing equipment and **b** photos of the meteorology sensors on the bow mast. **c** Schematics of the *NRV Alliance* looking down and in cross-section (CMRE 2017), with the marked instrument locations: radar (orange), lidar (blue), radiometer (purple), isotope container (red), ship's in situ meteorology (black circle), and the Sea-Bird Scientific digital oceanographic thermometer (green). (Color figure online)

and the radar were placed on the starboard side of the crew deck  $\approx 10$  m above sea level and the spectrometer was operated from the isotope container. Radiosondes (RS41, Vaisala, Vantaa, Finland) were launched from the ship at least every 24 h with high-frequency launches throughout intensive observational periods. During the first 24 h of the evaluated CAO event, for example, radiosondes were launched every 3 h. Further specifications of the profiling instruments, in particular the vertical range (m above the respective instrument) and the vertical and temporal resolution, are summarized in Table 1.

## 2.2 Satellite Observations

We extract the spatial distribution of *SST* and sea-ice cover over the course of the IGP cruise displayed in Fig. 1b, as well as a series of *SST* along the track of the *NRV Alliance*, from the GHRSSST satellite product (JPL 2015). The dataset provides daily values at  $0.1^\circ \times 0.1^\circ$  spatial resolution. In addition, infrared and visible satellite images were collected and stored for a predefined domain in real time for the IGP field campaign by the Natural Environment Research Council Earth Observation Data Acquisition and Analysis Service. The images are available up to 35 times per day with a resolution of 500 m. We utilize one of these satellite images to display and evaluate the cloud situation, corresponding to the time and location marked by the red cross in Fig. 1b (see Sect. 4). The image used here is from the MODIS instrument aboard the NASA Aqua satellite.

**Table 1** Specification of the profiling instruments operated from the *NRV Alliance* during the IGP campaign

Instrument (Identifier)	Variables		Resolution		Dataset
	Direct	Retrieval	Time	Range	Reference
Lidar (WindCube)	$\mathbf{v}_r$ (m s <sup>-1</sup> )	$\mathbf{u}$ (m s <sup>-1</sup> )	0.26 Hz (every 3.8 s)	20 m (40–200 m) 30 m (200–290 m)	Duscha (2020)
Radiometer (HATPRO)	$T_b$ (K)	$T_a$ (K) $RH$ (%)	$1.67 \times 10^{-3}$ Hz (every 10 min)	Discretized to 10 m (0–3 km)	Brooks (2019a)
Radar (MRR)	$v_r$ (m s <sup>-1</sup> ) $Z_e$ (dBZ)		0.1 Hz (every 10 s)	75 m (75–2325 m)	Sodemann (2021)
Radiosonde (RS41)	$T_a$ (K) $RH$ (%) $z$ (m)	$P$ (hPa) $ws$ (m s <sup>-1</sup> ) $wd$ (°)	1 Hz (every 1 s)	5 m (up to 20000 m)	Brooks (2019b)

Documentation of the main evaluated variables (measured and retrieved), the temporal and vertical resolution of the instruments, and the reference to the data in the CEDA database. The vertical resolution is documented as range resolution, valid for a certain range (in brackets) above the respective instrument. The variables are defined in the text, with the exception of the radial velocity vector,  $\mathbf{v}_r$ , the brightness temperature,  $T_b$ , and the radar reflectivity,  $Z_e$ , directly observed by the remote-sensing instruments

## 3 Methodology

### 3.1 Boundary-Layer Diagnostics

Based on the variables obtained from the ship-installed and ship-launched instrumentation, we estimate several diagnostics that characterize the structure of the MABL. Many of these diagnostics require a profile of potential temperature,  $\theta(z)$ , which we estimate from  $T(z)$ , and  $p(z)$ , obtained by the radiometer and the radiosondes, respectively. We also calculate the local lapse rate,  $\Delta\theta/\Delta z$ , using  $\Delta z = 100$  m, with the respective level,  $z$ , in the centre. We estimate  $\Delta\theta/\Delta z$  in overlapping intervals every 10 m, starting at  $z = 50$  m above sea level.

#### 3.1.1 Convective Boundary-Layer Depth

The MABL is the layer of the atmosphere that is directly impacted by ocean surface fluxes. It is hence characterized by the presence of mechanically and thermally generated turbulence. During marine CAO events a convective boundary layer develops. In this case the maximum depth of the turbulent convective motion, initiated at the sea surface, predominantly determines the depth of the mixed layer and hence the depth of the MABL. Utilizing the parcel method (Holzworth 1964), we determine the convective boundary-layer depth,  $h_b$ . The method relies on the principle of adiabatically following an air parcel from the sea surface, where  $\theta = \theta_{SST}$ , to its height of neutral buoyancy. The level that precedes the first instance of  $\theta(z_j) - \theta_{SST} \geq 0$  K, so the level  $z_{j-1}$ , is defined as  $h_b$

$$h_b = z_{j-1} |_{(\theta(z_j) - \theta_{SST}) \geq 0 \text{ K}}$$

The parcel method has been found to work well for convective conditions (Seibert et al. 2000). Additionally, Collaud Coen et al. (2014) found very good agreement of the convective boundary-layer depth between radiometer and radiosonde estimates, utilizing the parcel method. The uncertainty of  $h_b$ , in particular for the radiometer, was found to be most sensitive to the accuracy in the measurement of sea-surface temperature, which is within  $\pm 0.5$  K

(Collaud Coen et al. 2014). The value of  $h_b$  additionally serves as a measure of the potential maximum vertical extent of convective structures.

### 3.1.2 Gradient Richardson Number

Even though convective conditions usually predominate during marine CAOs, we still expect wind shear to have a strong influence on turbulence generation. To evaluate the dominant source of near-surface turbulence, we estimate the discretized, near-surface gradient Richardson number,  $Ri_g$  (e.g., Stull 1988)

$$Ri_g = \frac{g}{\theta} \frac{\Delta\theta/\Delta z}{[(\Delta u/\Delta z)^2 + (\Delta v/\Delta z)^2]}$$

with  $g$  being the the acceleration due to gravity. Here, we estimate  $Ri_g$ , centred at  $z = 100$  m above sea level, utilizing lidar observations of  $u$  and  $v$  at 50 m and 150 m above sea level in order to estimate the corresponding velocity gradients. We average the lidar estimates over 10 min to match the time resolution of the radiometer estimates of  $\theta(z)$  and the lapse rate between 50 m and 150 m above sea level.

### 3.1.3 Updraft and Downdraft Velocities

To evaluate the strength of the near-surface turbulent circulation, we estimate the maximum updraft and downdraft velocity,  $w_{\max}^{\uparrow}$  and  $w_{\max}^{\downarrow}$ , from lidar observations of the vertical velocity component,  $w$ . We evaluate the positive and negative  $w$  as two separate time series, using absolute values. For both the updraft and downdraft series we estimate the value of maximum velocity over the whole lidar altitude range at each timestep. We average the resulting series of maximum updraft and downdraft velocities over a 10-min interval to again match the time resolution of the radiometer.

### 3.1.4 Stable Water Isotope Composition

Cold-air outbreak events feature large humidity gradients and high wind speeds, which lead to intense evaporation from the sea surface (e.g., Papritz and Pfahl 2016). Under such conditions, the stable water isotopes  $\text{H}_2^{18}\text{O}$  and HDO (deuterium-enriched water) carry a specific signature in the evaporating vapour. We use this isotopic signature here as an integrating process tracer. More specifically, in intense evaporation conditions, the comparably higher diffusion speed of the HDO molecules compared to  $\text{H}_2^{18}\text{O}$  molecules leads to relatively high values ( $> 15 \text{ ‰}$ ) of the secondary isotope parameter  $d$ -excess ( $d$ ) defined as

$$d = \delta D - 8 \delta^{18}O,$$

where  $\delta D$  and  $\delta^{18}O$  denote the deuterium and oxygen-18 abundance in the water vapour relative to VSMOW (Vienna Standard Mean Ocean Water, e.g., Dansgaard 1964). Generally,  $d$  in water vapour is close to  $10 \text{ ‰}$  on a global average, and tends towards lower values as ambient conditions approach saturation (e.g., Pfahl and Sodemann 2014). The particular use of the parameter  $d$  in the context of this study is its ability to integrate over the evaporation history and mixing processes of water vapour in an airmass along its trajectory. Within a CAO, the local, high  $d$  signal from intense evaporation can be moderated by convective overturning of the MABL that transports comparably dry air with low  $d$  vapour, originating from heights dominated by condensation or from outside of the CAO to the surface. The isotope data are available in the CEDA archive (Sodemann and Weng 2022).

### 3.1.5 Fetch

Apart from the temporal evolution, the ship-based observations also describe a spatial evolution of the boundary-layer parameters, as the ship moves. This spatial evolution can be quantified by the fetch,  $f$  (km), the distance to the sea-ice edge, following the trajectory of the wind. Here, we estimate the fetch on the basis of the sea-ice edge from the GHRSSST sea ice product and the locally observed  $wd$ , which is varied by  $\pm 5^\circ$  to achieve an uncertainty estimate.

### 3.1.6 Surface Heat Fluxes

Turbulent sensible and latent heat fluxes,  $Q_H$  and  $Q_L$ , are a measure of the local energy transport of heat and moisture between the ocean and the atmosphere due to turbulent atmospheric motion. We determine these surface fluxes from the ship's meteorological observations (see Barrell and Renfrew 2020; Renfrew et al. 2021) using the well-established COARE 3.0 bulk flux algorithm (Fairall et al. 2003).

## 3.2 Coherent Structures

During CAO conditions, convective structures are superimposed on to the mean wind speed,  $\overline{ws}$ . For this study, we rely on the assumption that these structures are stationary, or "frozen", when sampled (i.e., Taylor's hypothesis). Also, the presence of advection or movement of the ship is a requirement to capture the convective signal with the lidar. Relative to the ship, convective structures are transported by the mean apparent wind speed,  $\overline{ws}_a$ , which results from the sum of  $\mathbf{u}$  and the ship's translational velocity vector,  $\mathbf{u}_{ship}$ . We apply a rolling average for  $\overline{ws}$  and  $\overline{ws}_a$  (local Taylor hypothesis). We chose a rolling average of 1 h, as it captures the synoptic and the diurnal variations in the flow, but filters variations due to convective structures  $\leq O(10^4 \text{ m})$  for the range of apparent wind velocity scales of  $O(10 \text{ m s}^{-1})$ , obtained during the CAO event. The coherent signal of convection needs to be evaluated along the mean apparent wind direction,  $\overline{wd}_a$ . So we rotate  $\mathbf{u}$  into  $\overline{wd}_a$  and subtract  $\overline{ws}$  from the rotated  $u$  component to obtain the along-wind, cross-wind, and vertical velocity fluctuations,  $u'$ ,  $v'$ , and  $w'$ , respectively.

$$\begin{pmatrix} u' \\ v' \\ w' \end{pmatrix} = \begin{pmatrix} \cos(\overline{wd}_a) & \sin(\overline{wd}_a) & 0 \\ -\sin(\overline{wd}_a) & \cos(\overline{wd}_a) & 0 \\ 0 & 0 & 1 \end{pmatrix} \begin{pmatrix} u \\ v \\ w \end{pmatrix} - \begin{pmatrix} \overline{ws} \\ 0 \\ 0 \end{pmatrix}$$

The series of the velocity fluctuations  $u'$ ,  $v'$ , and  $w'$  enable an estimate of the dynamic and spatial properties of coherent structures in the flow.

### 3.2.1 Cellular Structures

For a set of idealized convective cells, Fig. 3 illustrates how  $u'(t)$  and  $w'(t)$  would be observed by the ship-based lidar set-up at two altitude ranges,  $z_1$  and  $z_2$ . In this idealized case,  $u'(t)$  and  $w'(t)$  oscillate with the same period,  $T_{cell}$ . At both displayed levels, the two series are cross-correlated, but have a phase shift  $\Delta\rho_{u'w'} = \pm\pi/2$  ( $\pm 90^\circ$ ). The sign of  $\Delta\rho_{u'w'}$  is reversed for the upper and lower part of the cell. This is the case because the sign of  $w'(t)$  is conserved over the depth of the cell (lines overlap), while  $u'(t)$  switches sign from the



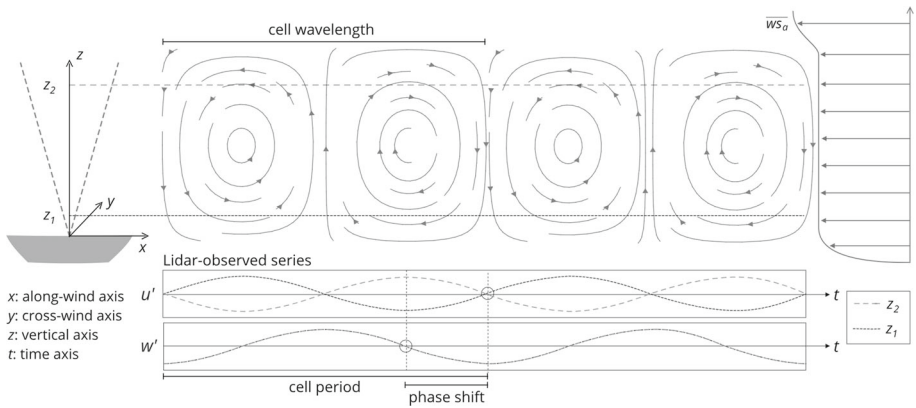


**Fig. 3** Schematic of the method utilized to observe cellular coherent structures with the ship-based lidar set-up. The top panel illustrates a cross-section through convective cells, along the mean apparent wind speed  $\overline{w_{s_a}}$ . The bottom panels show the series of  $u'(t)$  and  $w'(t)$  the ship-based lidar observes at two levels,  $z_1$  and  $z_2$ , when these cells are advected over the ship with  $\overline{w_{s_a}}$

lower to the upper part of the cell. The wavelength of the advected cell is proportional to the lidar-observed period ( $\lambda_{cell} \propto T_{cell} \overline{w_{s_a}}$ ).

Figure 3 displays only the two-dimensional, observational perspective from the ship-based lidar of a phenomenon that is three-dimensional in reality. In the idealized case, the convective cells are horizontally isotropic. Consider the case that the centre of such an isotropic cell is advected over the ship with  $\overline{w_{s_a}}$ . Here, the amplitude,  $u'_A$ , of the observed  $u'$  is maximal, while the amplitude,  $v'_A$ , of the observed  $v'$  is zero. Now consider the case that a cell is advected over the ship at a certain distance to its centre. Here, we expect to observe a contribution of the cellular circulation to  $v'_A$ . In contrast to the  $u'$  series, which is phase-shifted to  $w'$  by  $\pm\pi/2$  (Fig. 3), the corresponding  $v'$  series is instead anti-correlated to  $w'$ , hence phase-shifted by  $\pi$ . The ratio between  $v'_A$  and  $u'_A$  increases if the cell is sampled at an increasing distance to its center and this ratio can even exceed 1. Yet, the absolute values of  $u'_A$  and  $v'_A$  decrease towards the cell's edges rendering the coherent signal less reliable. Only if the cell passes the ship at approximately half the distance between its centre and edge is  $v'_A$  expected to yield a considerable coherent signal. Thus, in contrast to  $u'$ , the evaluation of  $v'$  is only reliable if a comparably narrow segment of the subsequent cells passes over the ship. This narrow segment is more likely to be missed by our set-up, compared to the larger segment relevant to the analysis of  $u'$ . Therefore, we focus our investigation on the estimation of the coherent signal between  $u'$  and  $w'$  to identify cellular coherent structures with the ship-based set-up.

### 3.2.2 Spectral Analysis

Based on the assumptions presented above, a measure of cross-correlation between the series of  $u'$  and  $w'$ , and a corresponding estimate of the phase shift for a range of periods or wavelengths can provide information about the presence of convective structures in the flow, including their respective  $T_{cell}$  and  $\lambda_{cell}$ . The coherence spectrum  $CO_{u'w'}$  is a measure for normalized cross-correlation between  $u'$  and  $w'$  (Emery and Thomson 2001)

$$CO_{u'w'} = \frac{G_{u'w'} \cdot G_{u'w'}^T}{G_{u'u'} \cdot G_{w'w'}}$$

where  $G_{u'w'}$  is the cross-covariance spectrum of  $u'$  and  $w'$ , and  $G_{u'w'}^T$  its complex conjugate. Further,  $G_{u'u'}$  and  $G_{w'w'}$  are the auto-correlation spectra of  $u'$  and  $w'$ , respectively. The  $Co_{u'w'}$  takes on values between 0 and 1, where 0 implies that  $u'$  and  $w'$  are not correlated, while 1 implies that  $u'$  and  $w'$  are correlated for a certain period or wavelength. If coherent structures are present in the flow, we expect to detect a spike in the  $Co_{u'w'}$  at  $T_{cell}$  or  $\lambda_{cell}$ , respectively. A spike in the  $Co_{u'w'}$  is the necessary condition for the presence of coherent structures. The corresponding sufficient condition is the presence of a phase shift of  $\pm\pi/2$  between  $u'$  and  $w'$  at the spike in the  $Co_{u'w'}$  (see Sect. 3.2.1). The phase spectrum  $\rho_{u'w'}$  is defined as follows (Emery and Thomson 2001)

$$\rho_{u'w'} = \text{atan2}[\text{Im}(G_{u'w'}), \text{Re}(G_{u'w'})].$$

With  $Co_{u'w'}$  and  $\rho_{u'w'}$  we can identify if coherent structures are superimposed on to the mean flow and estimate their horizontal length scale,  $L_{h,c}$ , along  $\overline{wd_a}$ .

### 3.2.3 The Coherent Length Scale

We found that the periodicity of the convective structures is sensitive to temporal changes in  $\overline{ws_a}$ , which can cause corresponding spikes in the frequency dependent  $Co_{u'w'}$  to widen and reduce in maximum value. A reliable interpretation of convection in the time domain is therefore not given (Lohse and Xia 2010). Hence, we convert both  $u'(t)$  and  $w'(t)$ , from a time to a space dependent series,  $u'(x)$  and  $w'(x)$ , using an approach based on the local Taylor hypothesis (see Pinton and Labbé 1994). We construct the space index,  $x$  (m), which describes the increasing distance covered along  $\overline{wd_a}$ , by multiplying the timestep  $\Delta t = 3.8$  s of the lidar observations with  $\overline{ws_a}(t)$  (m s<sup>-1</sup>) and integrate over  $t$ ,

$$x(t) = \sum_0^t \Delta t \overline{ws_a}(t).$$

We then rearrange the resulting  $u'(x)$  and  $w'(x)$  series to an equidistant grid. We chose a grid resolution of 50 m, to avoid aliasing effects at scales of  $O(10^2)$  m. We then split the series into a number of independent segments to capture the evolution of coherent structures. For a robust spectral analysis, the evaluated segment should contain at least five to ten cycles of the convective circulation. The length of the chosen segment should therefore be at least five times longer than the maximum coherent length scale of interest. For increasing scales the assumption of stationarity is less likely to be applicable and the application of the local Taylor hypothesis limits the maximum detectable structures to  $O(10^4)$  m. We utilize the  $u'$  and the  $w'$  series in segments of 100 km length to estimate  $Co_{u'w'}(\lambda)$  and  $\rho_{u'w'}(\lambda)$ . Here, each segment overlaps the next evaluated segment by 90 km, to ensure the detection of the large structures, which only persist at a constant scale for a limited number of consecutive structures throughout the observations. For each segment, this yields  $Co_{u'w'}(\lambda)$  and  $\rho_{u'w'}(\lambda)$  for a range of  $\lambda$  between  $10^2$  m (Nyquist) and  $2 \times 10^4$  m (five cycles over 100 km). However, the coherent signal in the lidar observations can be attenuated by ship-motion, the post-processing procedure applied to the lidar data to remove the ship-motion signal, and the lidar measurement principle. For the maximum observed  $\overline{ws_a} \approx 20$  m s<sup>-1</sup> this limits the detectable structures to  $L_{h,c} > 400$  m along  $\overline{wd_a}$ . Even though coherent structures with  $L_{h,c} < 400$  m likely occur in the flow, it is difficult to detect them with the utilized set-up. Such scales will thus be under-represented in the structure statistics. For the range of obtained  $\overline{ws_a}$ , we expect to achieve robust coherent-structure statistics for  $L_{h,c}$  between  $4 \times 10^2$  m and  $2 \times 10^4$  m.

Each  $L_{h,c}$  can be traced back to a certain time interval, as  $x$  is a function of  $t$ . We can thereby estimate the temporal fraction of the CAO that is occupied by coherent structures of a certain  $L_{h,c}$ . We estimate this temporal fraction relative to the whole duration of the CAO period. Integrating this relative time fraction over the duration of the whole CAO period results in the occurrence (%) of the respective  $L_{h,c}$ . If a coherent-structure pattern of respective  $L_{h,c}$  would persist throughout the whole CAO period, it would correspond to a 100 % occurrence. The temporal occurrence of each  $L_{h,c}$  can be estimated for any given time interval of the CAO. Here, we use 10-min intervals, to match the resolution of the boundary-layer parameters. Note, for each  $Co_{u'w'}(\lambda)$  and  $\rho_{u'w'}(\lambda)$ , it is possible to identify several coherent circulation patterns of different scales, coexisting in the flow field. Consequently, each evaluated segment is not limited to only a single length scale,  $L_{h,c}$ , but can host a multitude of them and their occurrences need to be interpreted independently. To identify the respective  $L_{h,c}$ , which correspond to coherent structures, we first need to define thresholds for  $Co_{u'w'}(\lambda)$  and  $\rho_{u'w'}(\lambda)$ , which are representative for real convective circulation in the atmospheric flow.

### 3.2.4 Thresholds for Atmospheric Convection

Convective circulation in the atmosphere deviates from the ideal case displayed in Fig. 3. We neither expect  $u'(x)$  and  $w'(x)$  to be perfectly correlated nor phase shifted. We need to define thresholds for  $Co_{u'w'}$  and  $\rho_{u'w'}$  that ensure that we correctly identify convective structures in the flow. A spectral analysis of horizontal and vertical velocity fluctuations by Hartmann et al. (1997) yielded a maximum coherence  $\approx 0.9$  when sampling organized convection during CAO conditions. Hartmann et al. (1997) sampled the velocity fluctuations along an aircraft track, perpendicular to the convective circulation, hence with a similar perspective as for one altitude displayed in Fig. 3. Here, coherence was generally smaller than 0.7, at scales that did not correspond to convective motion. Also, Hartmann et al. (1997) found the phase shift to be very close to the theoretical value of  $\pm\pi/2$ . Orienting on the thresholds defined by Hartmann et al. (1997), we select all  $\lambda$  as corresponding  $L_{h,c}$  (Sect. 3.2.2), for which the following criteria apply

$$\begin{aligned} Co_{u'w'}(\lambda) &> 0.7, \\ 85^\circ &< |\rho_{u'w'}(\lambda)| < 95^\circ. \end{aligned}$$

These thresholds ensure an exclusive detection of atmospheric convective structures with high confidence.

### 3.2.5 Strength of the Convective Circulation

In addition to the auto and cross-correlation spectra, we estimate the amplitude spectra of  $u'$ ,  $v'$ , and  $w'$ . Hence, each identified coherent structure can be linked to its corresponding horizontal and vertical velocity amplitudes,  $u'_A(L_{h,c})$ ,  $v'_A(L_{h,c})$ , and  $w'_A(L_{h,c})$ . It should be noted that the velocity amplitudes are conservative estimates, as they depend on which part of the structure passes over the ship. The values of  $u'_A$  and  $w'_A$  are reduced if the intersect is closer towards the structures' edges.

## 4 Coherent Structures During a Cold-air Outbreak

We estimate  $u'$ ,  $v'$ , and  $w'$  from the motion-corrected and post-processed lidar observations obtained during the CAO. To demonstrate the methodology described in Sect. 3.2, we first

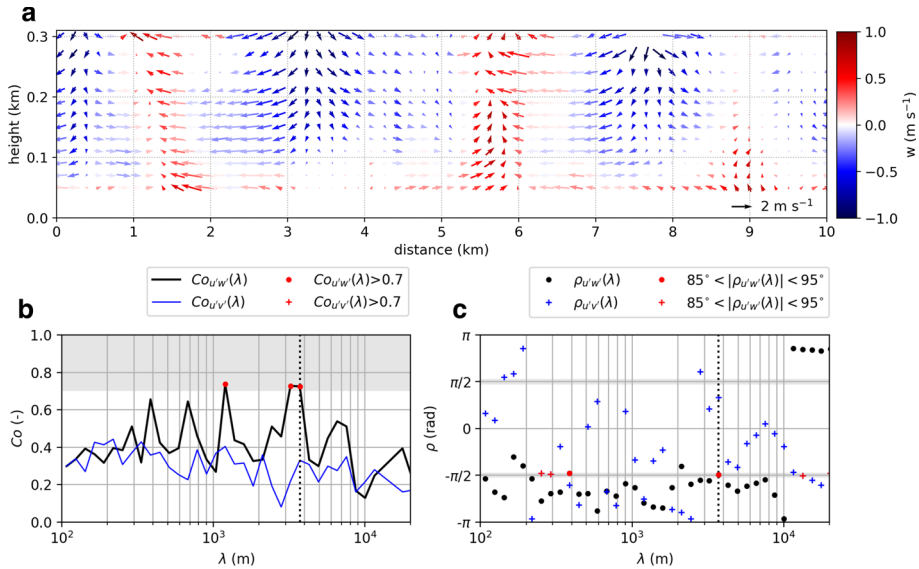


**Fig. 4** **a** Snapshot of the  $u'w'$  vector field retrieved from lidar observations, here displayed at an along-wind resolution of 200 m. **b** Corresponding coherence ( $Co$ ) spectra and **c** phase ( $\rho$ ) spectra calculated at 110 m above sea level obtained on 1 March 2018 at 0300 UTC. Grey shading highlights the range of  $Co$  and  $\rho$  where the criteria for coherent structures apply. Red markers indicate  $\lambda$  which fulfill the criteria in the displayed example. (Color figure online)

evaluate only a single exemplary situation. Here, we illustrate a convective situation, sampled on 1 March at 0300 UTC. Figure 4 displays the vector field of the  $u'$  and  $w'$  fluctuation, as well as the  $Co_{u'w'}(\lambda)$ ,  $Co_{v'w'}(\lambda)$ ,  $\rho_{u'w'}(\lambda)$ , and  $\rho_{v'w'}(\lambda)$  spectra.

The vector field displayed in Fig. 4a is dominated by wide, diverging downdrafts which feed the comparably narrow, converging updrafts. Such proportions in the convective updraft and downdraft are typically observed for open cells, which are dynamically driven from the bottom to the top (Salesky et al. 2017). In this 10-km-wide slice, approximately three wavelengths ( $L_{h,c} \approx 3 - 4$  km) of the lower part of the convective circulation pattern are represented. The convection pattern is level-consistent, except for one updraft around the 9 km mark, which does not penetrate as high. The corresponding coherence and phase spectra, estimated at 110 m above sea level, are displayed in Fig. 4b, c. The  $Co_{u'w'}$  spectrum shows three instances of  $\lambda$  where the  $Co_{u'w'}$  threshold is exceeded. As anticipated for cellular convection obtained by the ship-based lidar set-up (Sect. 3.2.1), the  $Co_{v'w'}$  spectrum features smaller values than the  $Co_{u'w'}$  spectrum and does not show the same distinct spikes. For the chosen example situation, the two criteria for the presence of a coherent-structure pattern defined in Sect. 3.2.4 apply for the coherence and phase spectra corresponding to the  $u'$  and  $w'$  series,  $Co_{u'w'}$ , and the  $\rho_{u'w'}$ , at  $\lambda \approx 3.7$  km. Hence, the spectral analysis method (Sect. 3.2.2), which identifies a pattern of convective structures of  $L_{h,c} \approx 3.7$  km, matches the visual evaluation corresponding to 3 to 4 km (Fig. 4a).

The large-scale cloud situation, obtained by the NASA Aqua polar orbiting satellite on 1 March 2018 at 0317 UTC, is shown in Fig. 5a. The satellite snapshot documents the cloud situation above the Iceland and Greenland Seas during the period relevant to the convective situation discussed above, representative for the early stage of the CAO. Surface pressure isobars and fronts from the U.K. Met Office's 0000 UTC analysis chart on 1 March were added

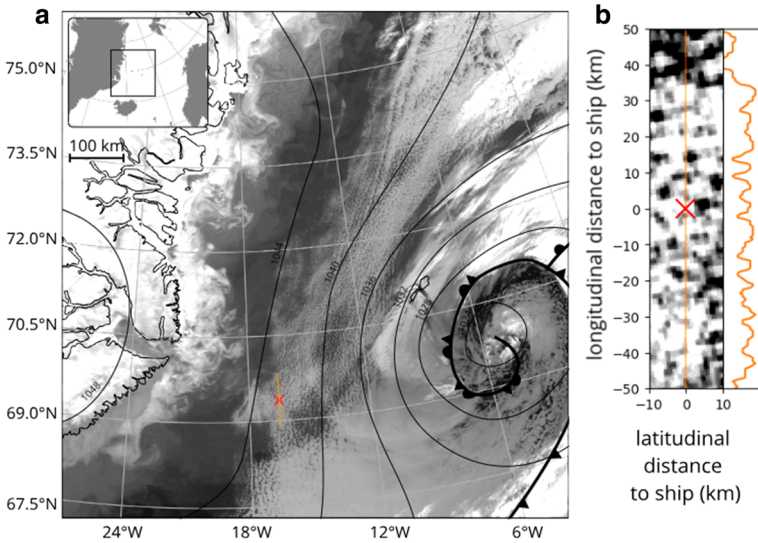


**Fig. 5** **a** Observations from MODIS on the NASA Aqua satellite, representing the cloud situation for the CAO on 1 March 2018 at 0317 UTC and surface pressure isobars and fronts, corresponding to the U.K. Met Office’s 0000 UTC analysis chart on 1 March 2018. **b** Close-up of the cloud pattern in the vicinity of the ship (red cross) and corresponding MODIS reflectance along the longitudinal cross-section (orange line). (Color figure online)

to document the synoptic situation. Here, the geostrophic flow is predominantly directed from north-north-east to south-south-west. Closer to the surface, the flow is expected to gain a more northerly component due to friction. This flow initiated the advection of cold and dry air from the sea-ice, which eventually initiated the onset of the CAO conditions in the Iceland and Greenland Seas region. The organization of the flow is connected to the passage of a cyclone through the area of the Iceland and Greenland Seas, a typical mechanism for the genesis of CAOs over high-latitude ocean areas (e.g., Fletcher et al. 2016). The area in the ship’s vicinity, marked by a red cross in Fig. 5a (see also Fig. 1a), is covered by cellular clouds. Figure 5b shows a close-up of this cloud pattern and the corresponding reflectance in the satellite observations, along the longitudinal cross-section at  $\pm 50$  km distance from the ship. Along the 100-km-long cross-section, we observe 13 single cellular clouds, which yields a corresponding cloud wavelength,  $\lambda_{cloud} \approx 7.7$  km. The horizontal cloud scale is therefore approximately twice as large as the  $L_{h,c}$  found from spectral analysis on 1 March at 0300 UTC of the near-surface range of the wind-profiling lidar (Fig. 4). Similar to findings presented by Renfrew and Moore (1999), this observation implies that every second convective cell, initiated near the surface and observed by the ship-based lidar (Fig. 4), manifested as a cloud, which can be identified from the satellite image (Fig. 5).

#### 4.1 Coherent-Structure Statistics

We now apply the methodology demonstrated above over the lifecycle of the CAO event and integrate the occurrence of each identified  $L_{h,c}$  over the entire evaluated period. Figure 6a shows the resulting occurrence for structures integrated over all the lidar levels. Note, individual structures that span the entire vertical lidar range are counted as one. Identified

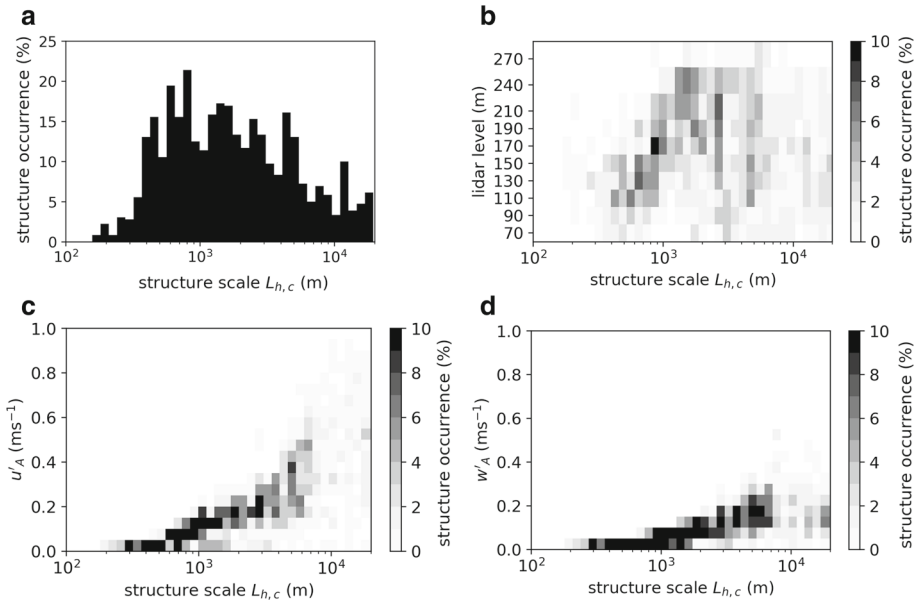


**Fig. 6** Coherent-structure occurrence, displayed versus  $L_{h,c}$  over the evaluated CAO period. The panels show **a** integrated  $L_{h,c}$  occurrence. **b**  $L_{h,c}$  occurrence per vertical lidar level. **c**  $L_{h,c}$  occurrence per  $u'_A$  interval. **d**  $L_{h,c}$  occurrence per  $w'_A$  interval

structures with  $L_{h,c}$  between  $4 \times 10^2$  m and  $6 \times 10^3$  m occur frequently. This is in line with the range of scales we expect to obtain with the ship-based lidar (Sect. 3.2.3). Coherent structures with  $L_{h,c} \approx 7 \times 10^2$  m are most frequently observed corresponding to  $\approx 20\%$  of the evaluated CAO period (Fig. 6a). Here, the occurrences of  $L_{h,c}$  at the individual lidar levels provide an interesting insight (Fig. 6b). For  $L_{h,c}$  smaller than  $2 \times 10^3$  m the identified  $L_{h,c}$  increase with increasing lidar level, explaining the frequent  $L_{h,c}$  occurrences at smaller scales (Fig. 6a). The increasing  $L_{h,c}$  with height, evident in Fig. 6b, indicates that only a fraction of the individual thermals observed at the lowest lidar levels reaches up to higher altitudes. We also observed this process during the investigation of the 10-km-wide wind fluctuation field (Fig. 4). If an individual thermal does not reach as high, the distance between the updrafts increases at higher altitudes and hence causes the identified  $L_{h,c}$  to increase. The formation of clouds with  $\lambda_{cloud}$ , identified to be twice the size of  $L_{h,c}$  at comparably lower altitudes (Fig. 4, Fig. 5), follows the same mechanism at larger scales. This mechanism was also reported in past CAO studies (e.g., Atlas et al. 1986; Renfrew and Moore 1999; Cook and Renfrew 2015). With increasing structure scales, e.g. at  $L_{h,c} \approx 2.5 \times 10^3$  m and  $L_{h,c} \approx 5 \times 10^3$  m, individual structures span the entire lidar range more frequently throughout the CAO event (Fig. 6b). Due to the higher occurrence of smaller  $L_{h,c}$ , identified at lower lidar levels, the corresponding  $L_{h,c}$  occurrence distribution features more distinct peaks than the occurrence of structures with the respective  $L_{h,c}$  at the higher levels (Fig. 6a, b).

Figure 6c, d show the respective dependency of  $u'_A$  and  $w'_A$  on  $L_{h,c}$ . Small coherent structures ( $L_{h,c} < 10^3$  m) contribute exclusively with small  $u'_A$  and  $w'_A$  ( $< 0.2$  m s $^{-1}$ ), i.e. reduced turbulent mixing in the MABL. With increasing  $L_{h,c}$ , the corresponding  $u'_A$  and  $w'_A$  increase. The velocity amplitude  $u'_A$  exhibits a stronger increase with increasing  $L_{h,c}$  than

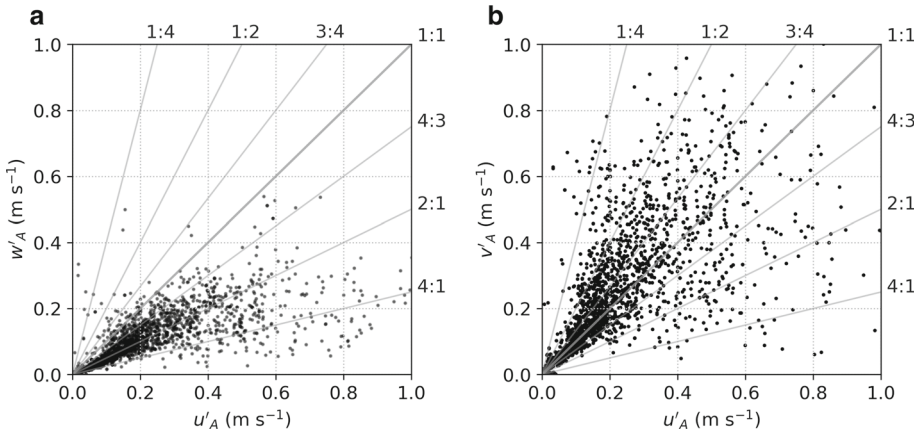


**Fig. 7** Scatter of  $u'_A$  against **a**  $w'_A$  and **b**  $v'_A$  corresponding to each coherent structure identified for the whole range of  $L_{h,c}$  and throughout the evaluated CAO period. Grey lines indicate the proportions between  $u'_A$  and  $w'_A$  and  $u'_A$  and  $v'_A$ , respectively

$w'_A$ . In fact,  $w'_A$  increases only until  $L_{h,c} \approx 8 \times 10^3$  m and remains at the same maximum value and velocity range for larger  $L_{h,c}$ . For  $L_{h,c} < 8 \times 10^3$  m,  $u'_A$  is mostly two to three times as large as the corresponding  $w'_A$ . These large differences are also apparent in the scatter of  $u'_A$  against  $w'_A$  for the whole range of obtained  $L_{h,c}$ , which is displayed in Fig. 7a. For the evaluated CAO event, the maximum observed amplitude of the vertical overturning of the MABL is capped at approximately  $0.5 \text{ m s}^{-1}$  (Figs. 6d, 7a). The velocity amplitude,  $u'_A$ , which compensates the vertical contribution to the convective circulation along-wind, reaches much larger values of up to  $1 \text{ m s}^{-1}$  (Figs. 6c, 7a). For small coherent structures and velocity amplitudes,  $u'_A$  and  $w'_A$  scatter around the 2:1 ratio (Fig. 7a). For increasing  $u'_A$ , which also correspond to larger  $L_{h,c}$  (Fig. 6c), the scatter of  $u'_A$  and  $w'_A$  is closer to the 4:1 ratio (Fig. 7a). An implication of this increasing ratio between  $u'_A$  and  $w'_A$  is that the ratio between  $L_{h,c}$  and the vertical coherent-structure depth also increases from small  $L_{h,c}$  to large  $L_{h,c}$ .

Figure 7b displays the scatter of  $u'_A$  against  $v'_A$  for the whole range of  $L_{h,c}$  over the evaluated CAO period. Note, we find a similar relationship between  $L_{h,c}$  and  $v'_A$  as for  $L_{h,c}$  and  $u'_A$  (not shown). The scatter between  $u'_A$  and  $v'_A$  is dense about the 1:1 ratio and mainly within the 1:2 and 2:1 ratios for small  $u'_A$  and  $v'_A$  (Fig. 7b), corresponding to  $L_{h,c}$ , which are predominantly smaller than  $2 \times 10^3$  m (Fig. 6c). A ratio close to 1 is within the range expected for horizontally isotropic cells. The velocity amplitudes,  $u'_A$  and  $v'_A$ , result from composites of several structures intersecting the ship's path at varying distance to their centre. For small  $L_{h,c}$ , a large number of structures resemble the corresponding coherent-structure pattern, representing average  $u'_A$  and  $v'_A$  over the different intersects (see Sect. 3.2.1). Neither  $u'_A$  nor  $v'_A$  represents the maximum strength of the structures, but rather average properties over the corresponding structure sizes. For increasing  $u'_A$  and  $v'_A$ , the spread of the scatter points increases (Fig. 7b). A relatively higher fraction of scatter points than for small  $u'_A$  or  $v'_A$  lies outside the 1:2 and 2:1 ratios, respectively. The larger spread at increasingly large velocity amplitudes corresponds to  $L_{h,c}$  larger than  $2 \times 10^3$  m (Fig. 6c). Here, the ship's intersection with a single large-scale structure strongly contributes to the corresponding values of  $u'_A$  and  $v'_A$  in contrast to a composite velocity amplitude of multiple small coherent structures.

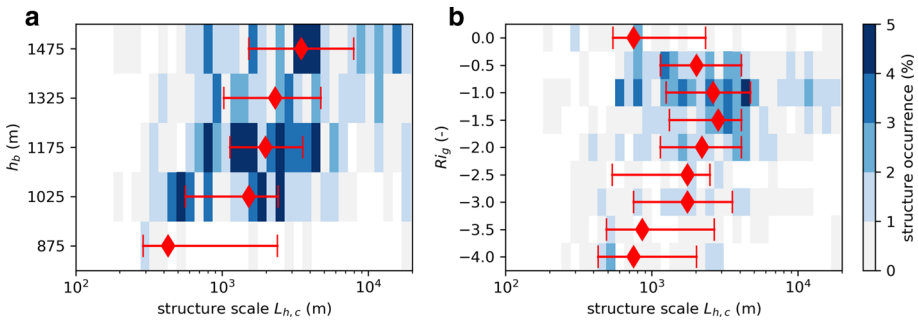


**Fig. 8** Occurrence of coherent structures of respective  $L_{h,c}$ , corresponding to the evaluated CAO period and integrated over **a**  $h_b$  range bins of 150 m between 800 m and 1550 m, **b**  $Ri_g$  range bins of 0.5, ranging from  $-4.25$  to  $0.25$ . Occurrences corresponding to structures outside of the displayed  $h_b$  and  $Ri_g$  ranges are counted to the corresponding lowest or highest range bins, respectively. For each bin of the corresponding boundary-layer parameter, the quartiles (25-percentile, median, 75-percentile) are indicated in red. The median is indicated by red diamonds and the interquartile range of  $L_{h,c}$  is indicated by the horizontal red line. (Colour figure online)

We now shift the focus of the discussion from the inter dependency of the coherent-structure characteristics to their dependency on the obtained boundary-layer parameters. Each boundary-layer parameter, introduced in Sect. 3.1, is separated into bins, corresponding to their respective uncertainty range. We combine the time series of the identified  $L_{h,c}$  and the time series of the boundary-layer parameters by integrating the temporal occurrence of each  $L_{h,c}$  over each of the boundary-layer bin ranges. Similar to the occurrence distribution displayed in Fig. 6a, we count a  $L_{h,c}$  that is simultaneously observed at several lidar levels as a single coherent-structure pattern. Hence, integrating the resulting  $L_{h,c}$  occurrence distribution over the whole range of the respective boundary-layer parameter would yield the same distribution as shown in Fig. 6a. Note, an integration of the occurrences over the range of  $L_{h,c}$ , on the other hand will not yield the occurrence of the boundary-layer parameter, because structures of different scales can coexist in the flow field. Figure 8 displays the  $L_{h,c}$  occurrences, corresponding to  $h_b$  and  $Ri_g$ , which show a noticeable dependency on  $L_{h,c}$  over the course of the evaluated CAO period.

Figure 8a shows the dependency of the  $L_{h,c}$  occurrences on  $h_b$  range bins. With increasing  $h_b$ , the occurrence distribution of  $L_{h,c}$  shifts to larger  $L_{h,c}$  values. Except for the lowest  $h_b$  bin between 800 m and 950 m, which includes only a small fraction of the  $L_{h,c}$  occurrence, the median  $L_{h,c}$  is in the range of  $\approx 2 \times 10^3$  m to  $4 \times 10^3$  m (2 to 4 km). The median  $L_{h,c}$  is approximately twice as large as  $h_b$  over the range of  $h_b$  between  $\approx 1$  km and 1.5 km. We observe similar values for the ratio between  $u'_A$  and  $w'_A$  displayed in Fig. 7a. Cieszelski (1998) sampled cellular convection, which featured a very similar horizontal extent of 2 km to 3 km at a comparable convective boundary-layer depth of 1 km. Cieszelski's observations corresponded very well with ratios between the horizontal and the vertical convective scales found in laboratory experiments of cellular Rayleigh–Bénard convection. Based on their size and ratios, we also expect the coherent structures obtained during this study to have properties which are similar to cellular Rayleigh–Bénard convection, such as their dependency on the temperature gradient in the flow.

The Richardson number  $Ri_g$  is a measure for the balance between buoyancy (temperature gradient) and shear (velocity gradient) in the boundary layer. For the evaluated CAO, we observe a distinct dependency between the  $L_{h,c}$ -occurrence distribution and the near-surface



$Ri_g$  (Fig. 8b). Here, the median  $L_{h,c}$  decreases with increasingly negative  $Ri_g \leq -2$ . This is in line with the development of Rayleigh–Bénard convection scales with increasing buoyant forcing observed in laboratory experiments (e.g., Hu et al. 1995). Figure 8b shows that the largest median  $L_{h,c} \approx 3 \times 10^3$  m are present at  $Ri_g$  between  $-1.75$  and  $-1.25$ , where the turbulence generation is weakly buoyancy dominated. For the  $Ri_g$  bin centred at  $-1$ , where the turbulence generation is equally balanced between buoyancy and shear, we observe the most frequent occurrence of coherent structures, which is consistently high over almost the whole range of  $L_{h,c}$ . This dense  $L_{h,c}$  occurrence is both due to the frequent occurrence of  $Ri_g$  around minus 1, and due to increased multi-scale characteristics of the coherent structures for this  $Ri_g$  range bin. For  $Ri_g \geq -1$ , medium  $L_{h,c}$  decreases with increasing  $Ri_g$ . Yet, the occurrence of  $L_{h,c}$  also decreases for the more shear-dominated conditions corresponding to  $Ri_g$  values around 0. For  $Ri_g \geq 0.5$  (not shown), we identify no  $L_{h,c}$ . This is mainly because this condition is sparsely present during the obtained CAO period. But we also do not expect to obtain coherent structures during increasingly stable conditions, for which past studies (e.g., Barthlott et al. 2007) predominantly report very small turbulent-structure scales  $< 2 \times 10^2$  m in the boundary layer. Such small-scale structures are unlikely to be resolved accurately with the observations available here. Positive  $Ri_g$  correspond to comparably small  $L_{h,c}$ , because structures are hindered to grow to large scale, while a positive lapse rate works against the structure's expansion. Yet, large negative  $Ri_g$  also correspond to comparably small  $L_{h,c}$ . On the contrary to positive  $Ri_g$ , however, vertical decoupling is a key mechanism for large negative  $Ri_g$  and the strong buoyant forcing enhances the emergence of individual thermals. In the absence of the suppressing, enhancing, or vertically restricting factors, turbulence conditions, which are balanced between buoyancy and shear, favour comparably increased  $L_{h,c}$ .

The boundary-layer parameters,  $w_{\max}^{\uparrow}$ ,  $w_{\max}^{\downarrow}$ ,  $Q_H$ ,  $Q_L$ , and  $d$  are not displayed in Fig. 8, as they exhibit a more complex dependency on  $L_{h,c}$  than  $h_b$  and  $Ri_g$ . The parameters are obtained during evolving synoptic conditions as well as from a moving ship, which results in both a temporal and a spatial perspective of the processes that shape the coherent structures during the CAO event. In the following section, we investigate this temporal and spatial development of the boundary-layer parameters, the connected predominating processes, and their impact on the coherent-structure development.

## 4.2 Coherent-Structure Evolution

The final shape of the  $L_{h,c}$ -occurrence distribution (Fig. 6a) depends on the temporal and spatial evolution of the coherent structures identified during the evaluated CAO period. The time series of the predominating  $L_{h,c}$  is now examined via Fig. 9a. Displayed are the time series of structures with respective  $L_{h,c}$  which occurred most frequently throughout the CAO. Figure 9b–f shows the complementing time series of the boundary-layer parameters. Additionally, Fig. 9g depicts the general evolution of  $T_a$ ,  $SST$ , and wind during the CAO and Fig. 9h shows the fetch, representative for the spatial evolution of the evaluated CAO from the ship's perspective.

We identify the first robust signal of coherent structures in the lidar observations shortly after an initial increase in  $h_b$ ,  $d$ ,  $Q_H$ , and  $Q_L$  (Fig. 9b, e, f). The increase of these parameters is due to the advection of cold air from the north, indicated by a drop in  $T_a$  (Fig. 9g). The fetch corresponding to these first hours of the CAO event is consistently fixed at  $f \approx 250$  km (Fig. 9h). Even though near-surface instability is increased, the turbulence generation and deepening of the boundary layer to 1 km is mainly shear-driven, indicated by a  $Ri_g$  close to

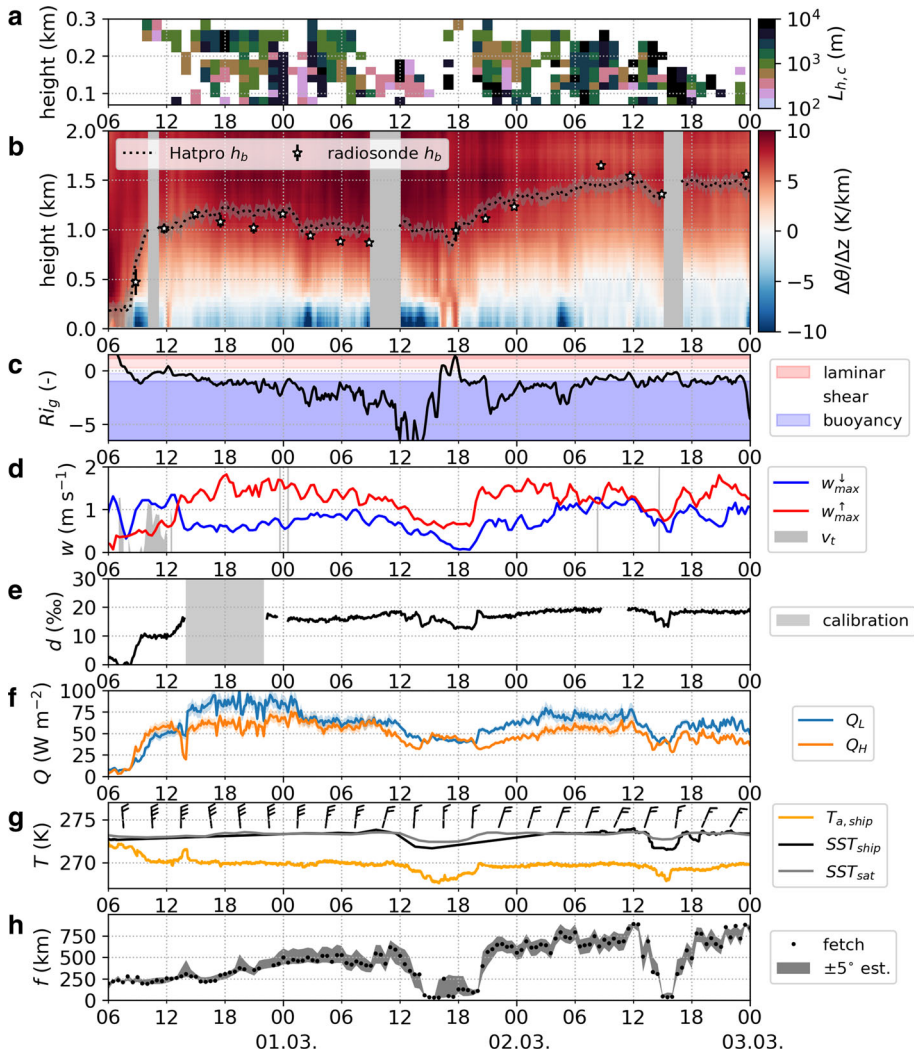


**Fig. 9** Time series of various variables obtained during the CAO period. **a** Hourly, most frequent  $L_{h,c}$ , obtained at different lidar levels. Timesteps, at which no coherent structures were identified are left blank. **b** Lapse rate  $\Delta\theta/\Delta z$  and buoyancy height  $h_b$  with corresponding uncertainty ranges from radiometer and radiosondes, with missing data marked in light grey. **c**  $Ri_g$  and indication of buoyancy-driven, shear-driven, and suppressed turbulence regime. **d** Time series of maximum velocities in up- and downdrafts. **e** Time series of  $d$ , with calibration periods shaded in grey. **f** Bulk sensible and latent heat fluxes  $Q_H$  and  $Q_L$  and corresponding uncertainty ranges. **g** Time series of  $T_a$ ,  $SST$  from ship and collocated along satellite observations of  $SST$ . Also wind barbs every 3 h, pointing in direction of the wind, with long feathers = 10 knots and short feathers = 5 knots. **h** Fetch,  $f$ , and corresponding  $wd \pm 5^\circ$  uncertainty range estimate. Note that 1 knot =  $0.514 \text{ m s}^{-1}$  [Ed.]. (Colour figure online)

zero (Fig. 9b, c). Remarkably, the evolution of  $h_b$ , estimated on the basis of the radiometer observation, is very close to those from the radiosonde measurements. During the first hours of the CAO, observations of small terminal velocities of precipitation ( $v_t \leq 1 \text{ m s}^{-1}$ , Fig. 9d) indicate the presence of snow-type precipitation (Maahn and Kollias 2012). Simultaneously increased  $w_{\max}^{\downarrow}$  and low  $w_{\max}^{\uparrow}$  values indicate an impact of this type of precipitation on the absolute vertical velocity observations by the lidar. Because an accurate observation of  $w$  is essential to estimate  $L_{h,c}$ , such a long period of precipitation potentially impacts the applicability of the spectral analysis method (Sect. 3.2.2), when the velocity fluctuations are dampened by the precipitation signal. This precipitation event also marks a halt in the otherwise monotonic increase of  $d$  from 0 ‰ to  $\approx 18$  ‰ at the beginning of the CAO (Fig. 9e). As long as  $d$  increases any convective overturning of the MABL is not sufficient to compensate for the increasing relative enrichment of HDO molecules in the water vapour, due to increased evaporation in the CAO conditions. Hence, along the whole distance between the ship and the origin of the CAO air masses ( $f \approx 250 \text{ km}$ ), the evaporation process at the sea surface provides a stronger isotopic signal than the mixing by convection. Unfortunately we cannot directly evaluate the observed trends in the boundary-layer parameters (Fig. 9b–f) in the context of  $L_{h,c}$  as no coherent structures could be detected during these first few hours (Fig. 9a). Assuming that precipitation does not conceal coherent-structure development, this indicates that the organization of coherent structures in the flow requires a certain spin-up time. This spin-up time is determined by the strength and speed of the cold-air advection.

From 28 February 1200 UTC, the evaluated CAO features organized convection, detectable with the spectral-analysis method introduced in Sect. 3.2. The predominating  $L_{h,c}$  gradually increase from  $O(4 \times 10^2 \text{ m})$  on 28 February 1200 UTC to  $O(10^4 \text{ m})$  on 1 March 0000 UTC and overall decrease again to  $O(4 \times 10^2 \text{ m})$  within 1 March 1200 UTC. On this comparably long time scale of 24 h, the boundary-layer parameters,  $h_b$ ,  $w_{\max}$ ,  $d$ , and  $Q$  show a response to the overall evolution of  $L_{h,c}$  (Fig. 9a–f). Yet a distinct, short-lived minimum  $L_{h,c} \approx O(4 \times 10^2 \text{ m})$  around 1 March 0200 UTC is not captured by these parameters. Here, only the near-surface instability and  $Ri_g$  (Fig. 9b, c) take increasingly negative values in correspondence. This observation confirms the sensitivity of  $L_{h,c}$  to  $Ri_g$  found in the  $Ri_g$ -dependent heatmap of  $L_{h,c}$  occurrences (Fig. 8b), while the other evaluated boundary-layer parameters show a less distinct relationship to  $L_{h,c}$ . The processes responsible for the evolution of the near-surface instability and  $Ri_g$  are therefore particularly interesting. On the short time scales, which are of interest to the evolution of  $Ri_g$ , changes in atmospheric conditions due to the ship's movement play a key role. From 28 February 1200 UTC to 1 March 0300 UTC  $f$  increases to  $\approx 500 \text{ km}$ , as the ship steamed to the south and away from the sea-ice edge (Fig. 1b, Fig. 9h). Along the way, on 1 March around 0000 UTC, the rain radar detects two short precipitation events with  $v_T > 2 \text{ m s}^{-1}$  (Fig. 9d), indicating that liquid droplets predominate during these events (see Maahn and Kollias 2012). With increasing fetch and time such precipitation events are expected to occur more frequently, as a response to the convective overturning of water vapour and cloud growth during the progressing CAO (e.g. Papritz and Sodemann 2018). Locally, evaporating precipitation can cause cooling in the near-surface layers. This can result in increased negative lapse rate and a stronger near-surface instability, which is observed when the ship moves into a location affected by precipitation. Cooling of the lower atmospheric layers can introduce vertical decoupling of the air-masses (Abel et al. 2017) and a corresponding restriction of the vertical structure scale and corresponding  $L_{h,c}$ , as observed on 1 March around 0200 UTC. Such decoupling is independent of the theoretical maximum vertical structure extension, represented by  $h_b$ . Except for the

near-surface instability and  $Ri_g$ , none of the boundary-layer parameters respond or can be identified as cause for the decreased  $L_{h,c}$  for this local, short-term mechanism.

After 1 March 0300 UTC the ship moves almost perpendicular to the wind direction and towards the sea-ice edge in the west (see Fig. 1b). Here, a second mechanism connected to the ship's movement impacts the evolution of  $Ri_g$ ,  $L_{h,c}$ , and most of the boundary-layer parameters. The fetch decreases and temporarily reaches a minimum around 1 March 1500 UTC (Fig. 9h). For a short fetch, the internal boundary layer initiated at the sea-ice edge is expected to be comparably shallow. Here, the value of  $h_b$  is not representative of the actual boundary-layer depth because it corresponds to that of a fully developed boundary layer, which is not present for such a short fetch. Within the shallow boundary layer the near-surface temperature gradient is steeper and coherent structures are restricted in vertical extent and hence in  $L_{h,c}$ , corresponding to a large negative  $Ri_g$ . With decreasing  $f$ ,  $Ri_g$ , and  $L_{h,c}$  (Fig. 9a, b, h), the strength of the vertical circulation,  $w_{\max}^{\uparrow}$  and  $w_{\max}^{\downarrow}$  and the turbulent fluxes,  $Q_H$  and  $Q_L$ , are correspondingly reduced (Fig. 9d, f). Also,  $d$  temporarily decreases from  $\approx 18\text{‰}$  to a local minimum of  $\approx 12\text{‰}$  (Fig. 9e). Here, the convective overturning of the MABL by predominantly small and weak convective structures is negligible and the structures' contribution to the exchange of near-surface air-masses exposed to evaporation is expected to be small. Hence, the sharp decrease in  $d$  can mainly be linked to the short fetch, as  $d$  results from an accumulated signal of the evaporation along the distance of the air-masses' trajectory. Large changes in  $f$  close to the spatial boundary of the CAO therefore yield the strongest concurrent impact of the ship's movement on the coherent-structure and the boundary-layer characteristics and need to be taken into account, when evaluating the event from a temporal perspective.

Over the lifecycle of the CAO, the predominantly northerly wind direction gains a small easterly component (Fig. 9g). This small change in wind direction causes an overall increase of the estimated  $f$  from  $\approx 250$  km at the onset of the CAO event to  $\approx 750$  km at the end of the evaluated period, independent of the ship's movement. There are two exceptions, where the ship's movement becomes apparent in a drop of  $f$ , on 1 March from 1200 UTC to 2100 UTC, which is discussed in the preceding paragraph and on 2 March from 1200 UTC to 1800 UTC, respectively. Following the overall trend of  $f$ , we identify the largest predominating coherent structures, corresponding to  $L_{h,c}$  of  $O(10^3)$  m to  $O(10^4)$  m more frequently towards the end of the evaluated CAO period. Also  $h_b$  increases from around 1 km in the first half to around 1.5 km in the second half of the evaluated CAO period, for which the near-surface lapse rate approaches zero. Notably, the trend identified for the overall evolution in  $f$ , the boundary-layer characteristics, and the coherent-structure characteristics is present for two periods corresponding to 1 March around 0600 UTC and 2 March around 0800 UTC. These two periods represent almost the same point in space, yet are separated by 26 h in time. Thus, temporal evolution and maturing of the CAO event impacts the evolution of the boundary-layer parameters and the corresponding coherent-structure characteristics. In contrast to the rapid changes observed for spatial changes, the temporal CAO evolution has a more moderate impact on the boundary-layer and the coherent-structure development.

For several of the boundary-layer parameters, we identify a long-term evolution, which can be linked to the coherent-structure characteristics. For periods during which we observe a coherent signal, we predominantly observe  $w_{\max}^{\uparrow}$  larger or equal to  $w_{\max}^{\downarrow}$  (Fig. 9d). This implies that the turbulent circulation generally features strong, but narrow updrafts and wider, but generally weaker downdrafts. Such a behaviour of the wind field is already depicted in Figure 4. Throughout the CAO, the estimated coherent vertical velocity amplitudes (Fig. 6d) correspond to approximately 10% of the sum of maximum updraft and downdraft veloci-

ties (Fig. 9d). In the presence of predominantly large-scale coherent structures,  $d$  remains mostly constant. Coherent structures are an important driver of the convective turnover of the MABL and hence work against the increase of  $d$  in the near-surface layers. During CAO conditions with large humidity gradients in the near-surface layer, a constant  $d$  implies that the enrichment of HDO due to evaporation is balanced by the convective overturning, which exchanges the air in the near-surface layer with comparably dry air from higher atmospheric levels. Here,  $d$  reaches maximum values of 18 ‰ to 20 ‰ throughout the evaluated CAO period. To maintain such moderately high values of  $d$ , in the presence of strong turnover of the MABL, a large humidity gradient is required above the water surface along the trajectory of the CAO air masses. According to the empirical relation of Pfahl and Sodemann (2014), the relative humidity above the water surface needs to be  $\approx 60\%$  on average along the trajectory, when calculated with respect to the measured  $SST$ , to yield such a value of  $d$ . The humidity and temperature gradients we observe during the CAO period result in turbulent heat fluxes. In comparison to previously studied CAOs, however, the turbulent heat fluxes obtained during the evaluated CAO event are relatively weak. Yet, the heat fluxes are elevated during periods, where large-scale coherent structures predominate relative to periods where small-scale coherent structures predominate. Hence, the coherent structures and large-scale overturning of the MABL have an impact on the overall evolution of  $Q_H$  and  $Q_L$ . The variations in  $Q_H$  and  $Q_L$  are, however, less sensitive to the coherent-structure characteristics, than for example those in  $Ri_g$ . This implies that small-scale and non-coherent turbulence also has an impact on  $Q_H$  and  $Q_L$  in the CAO event evaluated here and the turbulent heat fluxes result from a complex composite of irregular turbulent structures and convectively driven coherent structures. On the long-term, large-scale coherent structures yield the largest contribution to the heat fluxes and overturning of the MABL.

## 5 Conclusions

We develop a novel methodology to identify coherent structures based on the velocity fluctuations in the atmospheric flow during CAO conditions. We utilize a ship-based, wind-profiling lidar, employed during the IGP campaign on board of the *NRV Alliance*. We estimate the characteristics of the convective structures, and evaluate their interplay with other boundary-layer parameters. The ship-based approach captures the long-term statistics of the structure characteristics, an advantage over aircraft observations, which are limited to relatively short observational periods. In contrast to satellite snapshots, the ship-based approach provides a dynamical perspective on convection, and is able to determine coherent structures of multiple sizes in the flow simultaneously. Furthermore, the method does not require the formation of clouds in order to identify these structures and their corresponding characteristic spatial dimension.

The evaluated ship-based and multi-sensor set-up provides a detailed insight into the major processes revolving around coherent structures and the evolution of their characteristic size and strength in the MABL. Spectral analysis of the along-wind and vertical velocity fluctuations frequently yields a strong coherent signal throughout the lifecycle of the CAO. This indicates the organization of the convection into coherent structures. Each of these structures is linked to a characteristic horizontal length scale and an along-wind, cross-wind, and vertical velocity amplitude, under the assumption that isotropic cells predominate in the flow. The structures' characteristics identified for the evaluated CAO period match the characteristics expected for cellular convection. Over the course of the CAO event, the coherent structures feature variations in horizontal size and strength, which are sensitive to the near-surface

stratification and  $Ri_g$ . For unstable conditions, where turbulence generation is strongly dominated by buoyancy, small-scale structures ( $4 \times 10^2$  m) predominate. These structures are comparably weak and contribute little to the turbulent mixing in the MABL. We identify these small-scale structures more frequently in the lower lidar levels, while individual large-scale structures occur over the whole lidar range. Only a fraction of the individual thermals initiated at the surface occur throughout the lidar range and an even smaller number manifest as clouds. As shear-generated turbulence increases in importance, the size and strength of the coherent structures increases. Increasing median horizontal structure size of  $O(10^3)$  m coincides with increasing convective boundary-layer depth. The ratio between the median horizontal structure size and the boundary-layer depth is  $\approx 2$ . This ratio coincides with the median ratio found between the along-wind and vertical velocity amplitudes of the coherent structures. Throughout the evaluated CAO event the identified coherent convective structures mainly feature comparably wide and weak downdrafts and comparably narrow and strong updrafts. The largest coherent structures predominate for weakly buoyancy dominated conditions and for conditions equally balanced between buoyancy and shear-generated turbulence. For these large coherent structures, the size and horizontal velocity amplitude greatly exceed the vertical counterparts. The efficiency of the vertical overturning of the MABL is found to be capped for structures exceeding  $\approx 8 \times 10^3$  m for the evaluated CAO event. The overturning of the MABL compensates the near-surface enrichment of HDO, corresponding to the evaporation along the trajectory of CAO air-masses, yielding a maximum  $d$  between 18 ‰ and 20 ‰. Turbulent heat fluxes observed here are partly driven by small-scale and non-coherent turbulence and correspond to organized large-scale convective overturning by coherent structures only on long time scales. Short-term variations of the coherent-structure characteristics correspond almost exclusively to the near-surface stratification and  $Ri_g$ , which are mainly introduced by the ship's movement and the respective fetch.

The coherent structures discussed in this study correspond to one CAO case study obtained during the IGP campaign. The detailed observations of the velocity fluctuations provide the opportunity to further study the dynamics and direct impacts of the single or composite convective cells on the processes acting in the MABL. This can be particularly useful if additional observations of highly resolved boundary-layer processes are available. An example are the observations from additional platforms operated during IGP, such as a research aircraft, which provide overlapping observations corresponding to a few single convective structures. Investigating the observed structures in such detail will be the subject of a subsequent study. Yet to achieve statistics on coherent-structure characteristics applicable to the extensive range of CAO conditions in the Arctic, a larger observational basis is required. Such enhanced statistics on atmospheric convection during CAOs can, for example, be beneficial to model validation. Here, one should consider the utility of ship-based remote sensing, e.g., by ships of opportunity, which are operated in relevant but remote locations.

**Acknowledgements** This study was a part of the Iceland Greenland Seas Project. We are grateful for the constructive comments and insightful questions from the four anonymous reviewers, that helped to substantially improve the manuscript. We thank A. Seidl, A. Terpstra, S. Zou and Y. Weng for the set-up, maintenance and documentation of the ship-based instrumentation and measurements. We also thank M. Kähnert for helping with the formal editing and proofreading of the manuscript. J. Reuder acknowledges the Offshore Boundary Layer Observatory, OBLO, funded by the Research Council of Norway (NRF Grant No. 227777) for access to the WindCube V2 lidar system. H. Sodemann acknowledges the projects FARLAB (NRF Grant No. 245907) and SNOWPACE (NRF Grant No. 262710) for the stable water isotope instrumentation and measurements, respectively. The HATPRO and radiosounding system were provided by the Atmospheric Measurement and Observations Facility (AMOF) of the National Centre for Atmospheric Science (NCAS). The radiosondes were funded by the Atmospheric Forcing of the Iceland Sea project (AFIS) via the Natural Environment

Research Council (NERC) Grant NE/N009754/1, which also partly funded the contribution of I. Renfrew and C. Barrell to the study.

**Funding** Open access funding provided by University of Bergen (incl Haukeland University Hospital).

**Open Access** This article is licensed under a Creative Commons Attribution 4.0 International License, which permits use, sharing, adaptation, distribution and reproduction in any medium or format, as long as you give appropriate credit to the original author(s) and the source, provide a link to the Creative Commons licence, and indicate if changes were made. The images or other third party material in this article are included in the article's Creative Commons licence, unless indicated otherwise in a credit line to the material. If material is not included in the article's Creative Commons licence and your intended use is not permitted by statutory regulation or exceeds the permitted use, you will need to obtain permission directly from the copyright holder. To view a copy of this licence, visit <http://creativecommons.org/licenses/by/4.0/>.

## Appendix: Applicability to Mesoscale Convection and Roll Vortices

For the utilized ship-based lidar set-up, the presented methodology (Sect. 3.2) is restricted to estimates of  $L_{h,c}$  along the apparent wind direction,  $\overline{wd}_a$ . For a horizontally isotropic convective cell, the estimated  $L_{h,c}$  from spectral analysis directly represents its spatial extent. Yet, previous CAO studies (e.g., Atkinson and Zhang 1996; Hartmann et al. 1997; Renfrew and Moore 1999) report the presence of roll vortices, convective structures that have a much larger spatial extent along-wind than cross-wind. Due to this horizontal anisotropy, these structures need to be interpreted with care in terms of  $L_{h,c}$ . The longitudinal axis of rolls tends to align with a small angle,  $\alpha$ , to the mean wind direction. This is, for example, discussed by Atkinson and Zhang (1996), and evident in large-eddy simulations by Brilouet et al. (2020). Cross-wind movement of the ship can introduce an increased  $\alpha$ , relative to  $\overline{wd}_a$ . The roll circulation,  $v'_{roll}$ , perpendicular to the longitudinal roll axis, projected to  $u'_A$  and  $v'_A$  yields the following dependencies

$$\frac{u'}{v'_{roll}} = \sin(\alpha); \quad \frac{v'}{v'_{roll}} = \cos(\alpha) \quad \Rightarrow \quad \frac{u'}{v'} = \tan(\alpha).$$

When rolls are present in the flow and  $\alpha$  is small yet larger than  $0^\circ$  the coherent signal, obtained by the ship-based lidar, has a much larger contribution to  $v'_A$ , than to  $u'_A$ . The distribution of the ratio between  $u'_A$  and  $v'_A$  is expected to clearly shift to values close to zero. The  $v'$  series is proportional to  $v'_{roll}$ , which follows an analogous circulation with  $w'$  as illustrated in Fig. 3 in the cross-wind direction. The obtained  $v'$  for the roll case is thus phase-shifted by  $\pm\pi/2$  to the corresponding  $w'$ , in contrast to  $v'$  for isotropic cells. Hence, in the presence of roll vortices, one should also take  $Co_{v'w'}$  and  $\rho_{v'w'}$  into account as an criterion for the estimation of  $L_{h,c}$ . On the one hand,  $v'$  is expected to yield a much clearer coherent signal, at least for small  $\alpha$ . On the other hand, a corresponding phase shift between  $v'$  and  $w'$ , which is close to  $\pm\pi/2$ , provides the sufficient criterion that rolls are present in the flow. We tested this criterion for the evaluated CAO period, yet found no evidence that such anisotropic structures are present.

In the roll case, an estimate of  $L_{h,c}$  using the proposed method will correspond to the wavelength,  $\lambda'_{roll}$ , which describes the roll wavelength,  $\lambda_{roll}$ , transposed to the axis of  $\overline{wd}_a$

$$\frac{\lambda_{roll}}{\lambda'_{roll}} = \sin(\alpha).$$

The obtained  $L_{h,c}$  for rolls will be larger than the roll extent perpendicular to the longitudinal roll axis and smaller than the extent parallel to this axis.

## References

- Abel SJ, Boutle IA, Waite K, Fox S, Brown PRA, Cotton R, Lloyd G, Choullarton TW, Bower KN (2017) The role of precipitation in controlling the transition from stratocumulus to cumulus clouds in a northern hemisphere cold-air outbreak. *J Atmos Sci* 74(7):2293–2314. <https://doi.org/10.1175/JAS-D-16-0362.1>
- Achtert P, Brooks I, Brooks B, Moat B, Prytherch J, Persson O, Tjernström M (2015) Measurement of wind profiles by motion-stabilised ship-borne Doppler lidar. *Atmos Meas Tech* 8:4993–5007. <https://doi.org/10.5194/amt-8-4993-2015>
- Atkinson BW, Zhang JW (1996) Mesoscale shallow convection in the atmosphere. *Rev Geophys* 34(4):403–431. <https://doi.org/10.1029/96RG02623>
- Atlas D, Walter B, Chou SH, Sheu PJ (1986) The structure of the unstable marine boundary layer viewed by lidar and aircraft observations. *J Atmos Sci* 43(13):1301–1318
- Barrell C, Renfrew I (2020) Iceland Greenland seas Project (IGP): surface layer meteorological measurements on board the NATO research vessel Alliance. Centre for Environmental Data Analysis. <https://catalogue.ceda.ac.uk/uuid/b4ba8f11459c422d84d7293b9211ccf7>
- Barthlott C, Drobinski P, Fesquet C, Dubos T, Pietras C (2007) Long-term study of coherent structures in the atmospheric surface layer. *Boundary-Layer Meteorol* 125:1–24. <https://doi.org/10.1007/s10546-007-9190-9>
- Brilouet PE, Durand P, Canut G (2017) The marine atmospheric boundary layer under strong wind conditions: Organized turbulence structure and flux estimates by airborne measurements. *J Geophys Res Atmos* 122(4):2115–2130. <https://doi.org/10.1002/2016JD025960>
- Brilouet PE, Durand P, Canut G, Fourrié N (2020) Organized turbulence in a cold-air outbreak: Evaluating a large-eddy simulation with respect to airborne measurements. *Boundary-Layer Meteorol* 175(1):57–91. <https://doi.org/10.1007/s10546-019-00499-4>
- Brooks BJ (2019a) Iceland Greenland seas Project (IGP): Humidity and temperature profiles from the NCAS Humidity And Temperature PROFilers (HATPRO) scanning radiometer on board the alliance research vessel. Centre for Environ Data Anal. <https://catalogue.ceda.ac.uk/uuid/35f30876a4894169bb1ebeafe1e0c447>
- Brooks BJ (2019b) Iceland Greenland seas Project (IGP): Upper air sounding: Profiles of temperature, pressure, humidity, wind speed and wind direction. Centre for Environmental Data Analysis. <https://catalogue.ceda.ac.uk/uuid/5acca11ececbb4d8283b7e633370b6751>
- Brooks IM, Tjernström M, Persson POG, Shupe MD, Atkinson RA, Canut G, Birch CE, Mauritsen T, Sedlar J, Brooks BJ (2017) The turbulent structure of the arctic summer boundary layer during the arctic summer cloud-ocean study. *J Geophys Res Atmos* 122(18):9685–9704. <https://doi.org/10.1002/2017JD027234>
- Brümmer B (1996) Boundary-layer modification in wintertime cold-air outbreaks from the arctic sea ice. *Boundary-Layer Meteorol* 80:109–125. <https://doi.org/10.1007/BF00119014>
- Buckley MW, Marshall J (2016) Observations, inferences, and mechanisms of the Atlantic Meridional Overturning Circulation: A review. *Rev Geophys* 54(1):5–63. <https://doi.org/10.1002/2015RG000493>
- Chang SS, Roscoe Braham JR (1991) Observational study of a convective internal boundary layer over lake Michigan. *J Atmos Sci* 48(20):2265–2279
- Chou SH, Ferguson MP (1991) Heat fluxes and roll circulations over the western gulf stream during an intense cold-air outbreak. *Boundary-Layer Meteorol* 55(3):255–281. <https://doi.org/10.1007/BF00122580>
- Ciesielski R (1998) A case study of Rayleigh-Bénard convection with clouds. *Boundary-Layer Meteorol* 88(2):211–237. <https://doi.org/10.1023/A:1001145803614>
- CMRE (2017) NRV alliance drawings. Science and technology organisation centre for maritime research and experimentation, Tech rep
- Collaud Coen M, Praz C, Haeefe A, Ruffieux D, Kaufmann P, Calpini B (2014) Determination and climatology of the planetary boundary layer height above the Swiss plateau by in situ and remote sensing measurements as well as by the COSMO-2 model. *Atmos Chem Phys* 14(23):13,205–13,221. <https://doi.org/10.5194/acp-14-13205-2014>
- Cook P, Renfrew I (2015) Aircraft-based observations of air-sea turbulent fluxes around the British Isles: Observations of air-sea fluxes. *Q J R Meteorol Soc* 141:139–152. <https://doi.org/10.1002/qj.2345>
- Dansgaard W (1964) Stable isotopes in precipitation. *Tellus* 16(4):436–468. <https://doi.org/10.1111/j.2153-3490.1964.tb00181.x>
- Duscha C (2020) Iceland Greenland seas Project (IGP): three dimensional wind profile measurements from the University of Bergen Windcube V2 pulsed lidar on board the NATO research vessel Alliance. Centre Environ Data Anal. <https://catalogue.ceda.ac.uk/uuid/cc93b95c264644519777aa1ab37c23c0>



- Duscha C, Bakhoday-Paskyabi M, Reuder J (2020) Statistic and coherence response of ship-based lidar observations to motion compensation. *Journal of Physics conference series*. In: Proceedings of the 17th EERA DeepWind Conference, Trondheim, Norway <https://doi.org/10.1088/1742-6596/1669/1/012020>
- Emery WJ, Thomson RE (2001) Data analysis methods in physical oceanography - time-series analysis methods. Elsevier Science, chap 5:371–567. <https://doi.org/10.1016/B978-044450756-3/50006-X>
- Fairall CW, Bradley EF, Hare JE, Grachev AA, Edson JB (2003) Bulk parameterization of air-sea fluxes: Updates and verification for the COARE algorithm. *J Clim* 16(4):571–591
- Fletcher J, Mason S, Jakob C (2016) The climatology, meteorology, and boundary layer structure of marine cold air outbreaks in both hemispheres. *J Clim* 29(6):1999–2014. <https://doi.org/10.1175/JCLI-D-15-0268.1>
- Føre I, Kristjánsson JE, Sætra Ø, Breivik Ø, Røsting B, Shapiro M (2011) The full life cycle of a polar low over the norwegian sea observed by three research aircraft flights. *Q J R Meteorol Soc* 137(660):1659–1673. <https://doi.org/10.1002/qj.825>
- Grossman RL, Betts AK (1990) Air-sea interaction during an extreme cold air outbreak from the eastern coast of the United States. *Mon Weather Rev* 118(2):324–342
- Hartmann J, Kottmeier C, Raasch S (1997) Roll vortices and boundary-layer development during a cold air outbreak. *Boundary-Layer Meteorol* 84:45–65. <https://doi.org/10.1023/A:1000392931768>
- Holzworth GC (1964) Estimates of mean maximum mixing depths in the contiguous United States. *Mon Weather Rev* 92(5):235–242
- Hu Y, Ecke RE, Ahlers G (1995) Time and length scales in rotating Rayleigh-Bénard convection. *Phys Rev Lett* 74:5040–5043. <https://doi.org/10.1103/PhysRevLett.74.5040>
- JPL (2015) GHRSSST level 4 MUR Global Foundation Sea Surface Temperature analysis (v4.1), accessed 2020-01-27. <https://doi.org/10.5067/GHGM-R-4FJ04>
- LeMone MA (1973) The structure and dynamics of horizontal roll vortices in the planetary boundary layer. *J Atmos Sci* 30(6):1077–1091
- Lohse D, Xia KQ (2010) Small-scale properties of turbulent Rayleigh-Bénard convection. *Annu Rev Fluid Mech* 42(1):335–364
- Maahn M, Kollias P (2012) Improved micro rain radar snow measurements using Doppler spectra post-processing. *Atmos Meas Tech* 5(11):2661–2673. <https://doi.org/10.5194/amt-5-2661-2012>
- Papritz L, Pfahl S (2016) Importance of latent heating in mesocyclones for the decay of cold air outbreaks: a numerical process study from the pacific sector of the southern ocean. *Mon Weather Rev* 144(1):315–336. <https://doi.org/10.1175/MWR-D-15-0268.1>
- Papritz L, Sodemann H (2018) Characterizing the local and intense water cycle during a cold air outbreak in the nordic seas. *Mon Weather Rev* 146(11):3567–3588. <https://doi.org/10.1175/MWR-D-18-0172.1>
- Papritz L, Spengler T (2017) A lagrangian climatology of wintertime cold air outbreaks in the Irminger and Nordic seas and their role in shaping air-sea heat fluxes. *J Clim* 30(8):2717–2737. <https://doi.org/10.1175/JCLI-D-16-0605.1>
- Pfahl S, Sodemann H (2014) What controls deuterium excess in global precipitation? *Clim Past* 10:771–781. <https://doi.org/10.3929/ethz-b-000082937>
- Pinton JF, Labbé R (1994) Correction to the Taylor hypothesis in swirling flows. *J Phys II France* 4(9):1461–1468. <https://doi.org/10.1051/jp2:1994211>
- Renfrew IA, Moore GWK (1999) An extreme cold-air outbreak over the Labrador sea: Roll vortices and air-sea interaction. *Mon Weather Rev* 127(10):2379–2394
- Renfrew IA, Pickart RS, Våge K, Moore GWK, Bracegirdle TJ, Elvidge AD, Jeansson E, Lachlan-Cope T, McRaven LT, Papritz L, Reuder J, Sodemann H, Terpstra A, Waterman S, Valdimarsson H, Weiss A, Almansi M, Bahr F, Brakstad A, Barrell C, Brooke JK, Brooks BJ, Brooks IM, Brooks ME, Bruvik EM, Duscha C, Fer I, Golid HM, Hallerstig M, Hessevik I, Huang J, Houghton L, Jónsson S, Jonassen M, Jackson K, Kvalsund K, Kolstad EW, Konstali K, Kristiansen J, Ladkin R, Lin P, Macrander A, Mitchell A, Olafsson H, Pacini A, Payne C, Palmason B, Pérez-Hernández MD, Peterson AK, Petersen GN, Pisareva MN, Pope JO, Seidl A, Semper S, Sergeev D, Skjelvik S, Søyland H, Smith D, Spall MA, Spengler T, Touzeau A, Tupper G, Weng Y, Williams KD, Yang X, Zhou S (2019) The iceland greenland seas project. *Bull Am Meteorol Soc* 100(9):1795–1817. <https://doi.org/10.1175/BAMS-D-18-0217.1>
- Renfrew IA, Barrell C, Elvidge AD, Brooke JK, Duscha C, King JC, Kristiansen J, Cope TL, Moore GWK, Pickart RS, Reuder J, Sandu I, Sergeev D, Terpstra A, Våge K, Weiss A (2021) An evaluation of surface meteorology and fluxes over the Iceland and Greenland seas in ERA5 reanalysis: the impact of sea ice distribution. *Q J R Meteorol Soc* 147(734):691–712. <https://doi.org/10.1002/qj.3941>
- Salesky ST, Chamecki M, Bou-Zeid E (2017) On the nature of the transition between roll and cellular organization in the convective boundary layer. *Boundary-Layer Meteorol* 163:41–68. <https://doi.org/10.1007/s10546-016-0220-3>

- Seibert P, Beyrich F, Gryning SE, Joffre S, Rasmussen A, Tercier P (2000) Review and intercomparison of operational methods for the determination of the mixing height. *Atmos Environ* 34(7):1001–1027. [https://doi.org/10.1016/S1352-2310\(99\)00349-0](https://doi.org/10.1016/S1352-2310(99)00349-0)
- Sodemann H (2021) Iceland Greenland seas Project (IGP): precipitation measurements from the university of bergen micro rain radar (MRR2) on board the nato research vessel alliance. Centre for Environmental Data Analysis. <https://catalogue.ceda.ac.uk/uuid/dc723f82939843f199fff78778d5b8d0>
- Sodemann H, Weng Y (2022) Iceland-Greenland Seas Project (IGP): water isotope measurements from the University of Bergen vapour isotope analyzer on board the NATO Research Vessel Alliance within SNOWPACE. NERC EDS Centre for Environmental Data Analysis, 09 March 2022. <https://doi.org/10.5285/705abc2d9988444ba79e942f22219bc0>
- Stull RB (1988) An introduction to boundary layer meteorology. Springer, Dordrecht. <https://doi.org/10.1007/978-94-009-3027-8>
- Thurnherr I, Hartmuth K, Jansing L, Gehring J, Boettcher M, Gorodetskaya I, Werner M, Wernli H, Aemisegger F (2020) The role of air-sea fluxes for the water vapour isotope signals in the cold and warm sectors of extratropical cyclones over the southern ocean. *Weather Clim Dyn Discuss* 2020:1–42. <https://doi.org/10.5194/wcd-2020-46>

**Publisher's Note** Springer Nature remains neutral with regard to jurisdictional claims in published maps and institutional affiliations.